Observed Impact of Mesoscale Vertical Motion on Cloudiness

GEET GEORGE,[a] BJORN STEVENS,[a] SANDRINE BONY,[b] MARCUS KLINGEBIEL,[a] AND RAPHAELA VOGEL[b]

[a] *Max-Planck-Institut für Meteorologie, Hamburg, Germany*
[b] *LMD/IPSL, CNRS, Sorbonne University, Paris, France*

(Manuscript received 3 November 2020, in final form 9 March 2021)

ABSTRACT: We use estimates of mesoscale vertical velocity and collocated cloud measurements from the second Next-Generation Aircraft Remote Sensing for Validation campaign (NARVAL2) in the tropical North Atlantic to show the observed impact of mesoscale vertical motion on tropical clouds. Our results not only confirm previously untested hypotheses about the role of dynamics being nonnegligible in determining cloudiness, but go further to show that at the mesoscale, the dynamics has a more dominant control on cloudiness variability than thermodynamics. A simple mass-flux estimate reveals that mesoscale vertical velocity at the subcloud-layer top explains much of the variations in peak shallow cumulus cloud fraction. In contrast, we find that thermodynamic cloud-controlling factors, such as humidity and stability, are unable to explain the variations in cloudiness at the mesoscale. Thus, capturing the observed variability of cloudiness may require not only a consideration of thermodynamic factors, but also dynamic ones such as the mesoscale vertical velocity.

SIGNIFICANCE STATEMENT: Knowing how low clouds link to atmospheric circulation over a few hundred kilometers will reduce current uncertainties in the sensitivity of Earth's climate to warming. Such investigations have previously been limited by lack of circulation measurements at the mesoscale. However, using measurements now available from a recent field campaign over the tropical North Atlantic along with cloud measurements, we demonstrate how atmospheric vertical motion especially in the lower layers can influence the extent and structure of clouds. We find that the kinematics have a more dominant control on low-level cloudiness than conventionally studied thermodynamics. Our results show why it is important to focus attention to the circulation to improve our understanding of the variability in cloudiness.

KEYWORDS: Atmosphere; Clouds; Convergence/divergence; Vertical motion; Boundary layer; Cloud cover; Cumulus clouds; Subsidence; Dropsondes; Kinematics; Lidars/Lidar observations; Measurements; Microwave observations; Radars/Radar observations; Remote sensing; Satellite observations

1. Introduction

Understanding how low-level clouds respond to their environment can help reduce uncertainties in climate sensitivity estimates (Bony and Dufresne 2005; Zelinka et al. 2020). Tropical environmental conditions on the mesoscale (20–200 km) can change within a few hours to a day, whereas over the large scale, $O(1000)$ km, conditions can be expected to persist for multiple days. What controls cloudiness at the mesoscale is not as well investigated as what controls them at the large scale. This shortcoming is mainly due to a limited understanding of how the atmospheric state varies at the mesoscale, especially in terms of circulation, which in turn can be attributed to an absence of observations at such scales. Nevertheless, the clouds–circulation coupling from the cloud scale to the large scale is thought to be important for the strength of cloud feedbacks and consequently, for projecting the future climate (Bony et al. 2015). In this study, we aim to provide insights into how atmospheric circulation can influence tropical cloudiness at the mesoscale.

Predicting cloudiness for an air parcel a priori is simple, and can be linked directly to the occurrence of saturation. In the tropical boundary layer, saturation is primarily associated with ascending air, and therefore, it is necessary to understand what determines the intensity, the spatial distribution, and the vertical extent of coherent ascents. This amounts to determining what controls the shallow convective mass flux. Vogel et al. (2020) show that mass flux is regulated by environmental factors, primarily the mesoscale atmospheric vertical motion at cloud base. This suggests that clouds depend directly on mesoscale circulation features, and that the connection between the two may need to be accounted for when predicting cloudiness.

To study the influence of circulation on clouds, observational challenges have compelled previous investigations to use reanalysis data, and since these are more reliable over larger scales of time and space, such studies focus on the large scale (e.g., Bony et al. 2004; Stevens et al. 2007; Myers and Norris 2013; and others). An unequivocal finding from these studies is that pressure velocity (ω) in the free troposphere (e.g., at 500 and 700 hPa) can be used to separate cloudiness into regimes of

Denotes content that is immediately available upon publication as open access.

Klingebiel's current affiliation: Leipzig Institute for Meteorology, University of Leipzig, Leipzig, Germany.

Corresponding author: Geet George, geet.george@mpimet.mpg.de

DOI: 10.1175/JAS-D-20-0335.1

© 2021 American Meteorological Society. For information regarding reuse of this content and general copyright information, consult the AMS Copyright Policy (www.ametsoc.org/PUBSReuseLicenses).
Brought to you by MAX-PLANCK-INSTITUTE FOR METEOROLOGY | Unauthenticated | Downloaded 07/20/21 01:00 PM UTC

shallow convection (subsidence) and deep convection (ascent). Additionally, if lower-tropospheric stability (LTS) is considered, one can classify the shallow convection regimes into stratocumuli (stronger inversion) and trade wind cumuli (weaker inversion), as shown by Medeiros and Stevens (2009). Along with stability and kinematic factors such as ω, clouds are also shown to be strongly associated with other thermodynamic factors such as relative humidity (Slingo 1987) and sea surface temperature (SST; Qu et al. 2015), which themselves are influenced by kinematic factors (or motion field parameters).

Klein (1997) and Brueck et al. (2015), however, show that on scales of 5 days or shorter, these associations weaken significantly. Moreover, Nuijens et al. (2015a) show that while humidity, lapse rate, surface wind speed, and ω at 850 hPa (ω_{850}) together explain close to 56% of the monthly variance in cloud cover in the trade wind region, they account for only 24% of the daily variance. These results indicate that factors controlling clouds on longer time and larger space scales hold lesser influence at the shorter (hours to days) and finer (20–200 km) scales, and that other factors might be more dominant in controlling cloudiness therein. The importance of determining these day-to-day or scene-scale controls is further highlighted by the finding of Nuijens et al. (2015b), that more than 50% and 75% of the variability observed in low-level cloudiness occurs over time scales shorter than 1 and 5 days, respectively.

The influence of dynamics on clouds has been investigated by several studies, but these were mainly restricted to stratocumulus regimes and have only used reanalysis products to characterize the environment, especially circulation parameters. Mauger and Norris (2010), using a Lagrangian framework, show that factors such as large-scale divergence (D) at the surface and ω_{700} have a more instantaneous control (0–12 h) on stratocumulus clouds compared to thermodynamic factors like LTS and SST (12–48 h). They also find that strong subsidence at 700 hPa leads to a reduction in cloud fraction. Myers and Norris (2013) similarly show that for constant inversion strength, stratocumulus cloud fraction increases with weakening subsidence. de Szoeke et al. (2016) find a similar effect as in both previous studies on the subdaily time scale, wherein clouds away from the stratocumulus regimes increase in amount with ascent in the free troposphere (ω_{700}). These aforementioned findings imply that cloudiness might be enhanced by low-level convergence at the mesoscale—a hypothesis currently lacking observational evidence for shallow cumulus clouds. Moreover, Stevens and Brenguier (2009) point out that in contrast to thermodynamic factors, the role that dynamic factors such as divergence play in controlling cloudiness is uncertain and far from trivial, particularly on finer scales which are less strongly coupled to the large-scale thermodynamic environment. Thus, for determining tropical cloudiness at such scales, it appears necessary to test the hypothesis about low-level convergence enhancing cloud fraction and to understand how clouds are controlled by the mesoscale dynamics. The long-standing challenge though, has been in measuring said dynamics.

Some field campaigns such as the Barbados Oceanographic and Meteorological Experiment (BOMEX; Holland 1970) and the Atlantic Trade-wind Experiment (ATEX; Augstein et al. 1974) have successfully measured divergence previously. But their small number of measurement points over the large scale makes it difficult to establish the veracity of these measurements, particularly on the mesoscale. These were also best constrained by large-scale budgets on much larger space and time scales than would be relevant for the mesoscale. However, Bony and Stevens (2019), using recent measurements from the second Next-Generation Aircraft Remote Sensing for Validation campaign (NARVAL2; Stevens et al. 2019a), demonstrate that area-averaged mesoscale D and ω can be measured using horizontal wind observations from dropsondes launched along a circular path. With successive measurements within the same air masses and confirmation from high-resolution simulations, they show that the NARVAL2 vertical motion estimates are indeed ones that can be confidently used at the mesoscale, which we aim to study here.

The vertical motion estimates and the collocated cloud measurements from NARVAL2 make it possible to investigate shallow cumulus clouds in their immediate environment, where both the thermodynamics and dynamics are well characterized. We exploit this opportunity and study how ω at different levels in the atmosphere (i.e., in the moist layer, at 700 and 500 hPa) controls shallow cloudiness differently, thus providing insight into how the circulation influences cloudiness at the mesoscale.

The structure of the paper is as follows. We give a short description of the data used in section 2, along with the methodology of their analyses. In section 3, we provide a quantitative picture of the cloudiness sampled during the campaign. This is followed by a discussion of associations between cloudiness and mesoscale environmental factors in section 4. Here, we look at the impact that thermodynamics and dynamics have on cloudiness, and test if ω can potentially be used as a predictor of cloudiness. In section 5, we summarize our findings, provide implications thereof and give an outlook for future studies.

2. Data and methodology

a. Circle environments

The NARVAL2 campaign took place in August 2016 over the tropical North Atlantic—east of Barbados—and included 10 research flights (RF) flown with the High Altitude and Long Range aircraft (HALO; Stevens et al. 2019a). Five of these flights included segments flown in circular patterns with a mean diameter of ~175 km (circles, hereafter), along which dropsondes were launched approximately every 4–6 min. One of these circles during research flight RF10 was located in the extratropics at about 35°N, and is excluded from the study. Data from the remaining eight circles (a total of 137 dropsondes) form the basis for this study. Their location and timing is summarized by Fig. 1 and Table 1, respectively. Circles other than those during RF07 were flown in pairs of a clockwise and an anticlockwise round each. Here, we use the term "circle" to mean these circle pairs, unless specified otherwise. Stevens et al. (2019a) provide more information about the campaign and the instruments employed for measurements, and the circle flight strategy is explained in detail by Bony and Stevens (2019).

Brought to you by MAX-PLANCK-INSTITUTE FOR METEOROLOGY | Unauthenticated | Downloaded 07/20/21 01:00 PM UTC

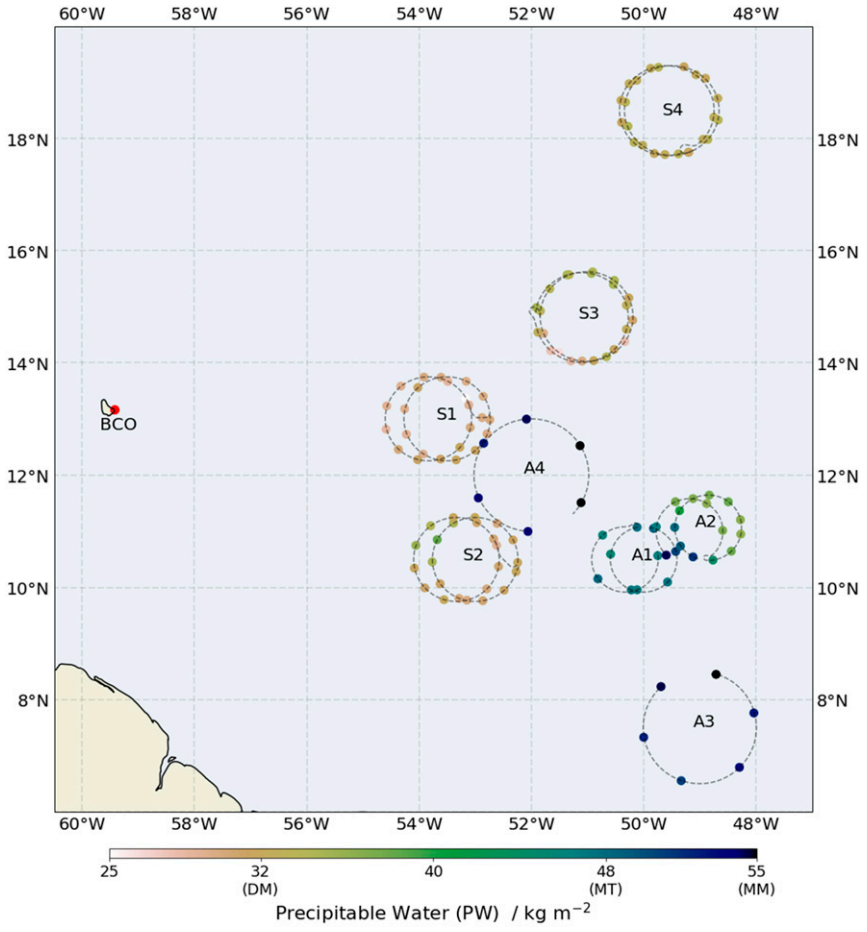

FIG. 1. Markers show dropsonde location for the different circles throughout NARVAL2, and are connected by the flight path during the circles. The marker colors indicate PW retrieved from the respective sondes. The red marker in the west shows the location of BCO. The color bar for PW indicates the labels of dry mode (DM), moist mode (MM), and the moist threshold (MT), used to categorize the circles (refer to the text in section 2b).

Vaisala RD-94 dropsondes were used during the campaign [refer to Wang et al. (2015) for details]. For processing the dropsonde raw data, we use the Atmospheric Sounding Processing Environment (ASPEN), version 3.3-297, software and interpolate the measurements to a uniform 10 m vertical grid. These processed data are used to estimate kinematic parameters such as D, ω, and vertical velocity (W) following Bony and Stevens (2019), as well as thermodynamic parameters such as static energy, precipitable water (PW), free-tropospheric humidity (FTH), surface wind speed, lifting condensation level (LCL), LTS, inversion height, and surface fluxes. PW and FTH are estimated as column water vapor from the surface and from the 700 hPa level, respectively, with the upper limit of the profile set to 5850 m, to be consistent with the lowest-flown circle. The surface wind speed is estimated as the mean of dropsonde measurements in the 50 m closest to the surface. We estimate the LCL using values of pressure, temperature and humidity averaged over the bottom 200 m and follow the method by Bolton (1980). LTS is defined as the difference between the potential temperature at 700 hPa and that at surface (10 m), following Klein and Hartmann (1993). For the inversion height, we use the height at which the squared Brunt–Väisälä frequency (N^2) has its first local maximum from the surface.

To estimate surface fluxes, we use dropsonde measurements of humidity, temperature, and wind speed at 20 m altitude, and apply the Coupled Ocean–Atmosphere Response Experiment (COARE) bulk flux algorithm version 3.6 as detailed in Fairall et al. (2003) and Edson et al. (2013). For SST, we use the nearest values from the European Centre for Medium-Range Weather Forecasts (ECMWF) reanalysis product [ERA5; Climate Data Store (CDS); CDS 2017; Hersbach et al. 2020] at 0.25° horizontal and 1 h temporal resolution.

b. *Classifying the circles*

The NARVAL2 circles sampled both deep and shallow convection. Here we refer to circles with deep convection and with profiles relatively closer to saturation as *active* circles (A-circles) and the circles with a substantially drier atmosphere

Brought to you by MAX-PLANCK-INSTITUTE FOR METEOROLOGY | Unauthenticated | Downloaded 07/20/21 01:00 PM UTC

TABLE 1. Details of the circles together with mean values of selected thermodynamic parameters. The dates are for August 2016 and the time is in UTC. Sondes are the total number of sondes launched in the circle for the clockwise (first number) and the counterclockwise (second number) rounds. Terms in the first columns are as follows: z_{flight} stands for mean flight altitude (m), u_{srf} stands for surface wind (m s^{-1}), LHF stands for latent heat flux (W m^{-2}), and z_{inv} stands for inversion height (m). The units for PW and FTH are in kg m^{-2}, whereas the units for LTS, SST, and LCL are K, °C, and m, respectively. Parameter definitions are given in section 2a. Note that due to the lack of a steady inversion, the inversion height value for A3 is unusually low and cannot be considered as an estimate for the true inversion height, like for the other circles. Numbers in parentheses are standard deviations.

	Flight ID							
	RF03		RF06		RF02		RF07	
Circle	S1	S2	S3	S4	A1	A2	A3	A4
Date	12	12	19	19	10	10	22	22
Diameter	167.37	168.08	177.37	176.99	133.24	131.46	221.42	221.62
Time	1354	1742	1433	1757	1407	1744	1537	1907
Sondes	12 + 12	12 + 12	12 + 12	13 + 11	6 + 6	11 + 6	6	6
z_{flight}	9024	9003	9035	9014	5894	5878	9011	8913
PW	29.4 (1.5)	31.4 (2.2)	31.0 (2.5)	32.1 (0.8)	46.9 (1.5)	40.2 (6.0)	50.1 (1.8)	52.3 (2.0)
FTH	4.3 (0.5)	4.5 (0.3)	3.0 (1.2)	1.9 (0.8)	8.4 (1.4)	4.5 (2.1)	12.4 (0.8)	10.1 (1.6)
LTS	14.1 (0.4)	13.3 (0.3)	14.7 (0.2)	13.5 (0.2)	13.0 (0.3)	13.5 (0.4)	11.3 (0.4)	13.6 (0.8)
u_{srf}	6.2 (0.4)	7.8 (0.3)	5.1 (0.2)	6.5 (0.2)	4.7 (0.3)	8.7 (0.4)	3.3 (0.4)	1.8 (0.8)
LHF	146.8 (26.7)	199.2 (26.5)	102.3 (19.8)	118.4 (16.2)	89.8 (13.2)	145.2 (39.4)	97.4 (57.7)	40.3 (7.7)
SST	28.4 (0.2)	29.4 (0.2)	27.9 (0.2)	28.1 (0.0)	29.0 (0.3)	28.8 (0.3)	29.8 (0.3)	28.7 (0.3)
LCL	795	865	730	675	590	590	720	510
z_{inv}	1390	1620	1650	1630	1400	1410	680	1630

and shallow convective activity as *suppressed* circles (S-circles).[1] We use mean PW of the circles (see Table 1) as a basis of classification. Mapes et al. (2018) set a PW moist threshold (MT) of 48 kg m^{-2} for deep convection. Their study also confirms the well-known bimodality in the distribution of tropical PW, and we associate their modes at lesser PW [~32 kg m^{-2}; dry mode (DM)] and at greater PW [~52 kg m^{-2}; moist mode (MM)] with the A- and S-circles, respectively. Note that the PW values in Mapes et al. (2018) were taken for the moisture in the entire atmospheric column, whereas the values here are for profiles only up to 5850 m, as explained in section 2a. For the circles with the moistest free troposphere (A3 and A4), the difference between estimating PW up to 5.85 km and up to flight altitude (9 km) is ~5%, while for all S-circles, this difference is ~1% or lesser. This confirms the general understanding about moisture in the trades, that there is very little moisture above 6 km. Therefore, we use the values from Mapes et al. (2018) as is, without any substantial impact on our separation of deep and shallow convection regimes.

Placing the NARVAL2 circles in the context of the above mentioned modes, we identify circles of RF07 as A-circles (A3 and A4) and those of RF03 and RF06 as S-circles (S1–S4), since their PW values match closely with the dry and moist modes, respectively. For the circles of RF02, this classification is a bit more delicate. Flight reports from the campaign confirm that they sampled the edge of deep convection areas, but in doing so also extended across airmass boundaries to include dry air masses. Thus, although PW values for some dropsondes in the RF02 circles are below the moist threshold (see Fig. 1), we classify them as A-circles (A1 and A2). In the nomenclature of the circles, the digits following the capitalized letters indicate the chronological sequence of the circles in their respective groups.

c. *Quantifying cloudiness*

1) AIRBORNE RADAR AND MICROWAVE MEASUREMENTS

To quantify cloudiness, we use the unified dataset by Konow et al. (2019) for measurements from the HALO Microwave Package (HAMP; Mech et al. 2014), which includes microwave radiometers and a 35 GHz cloud radar, all looking nadir from the aircraft. As we focus here on low-level clouds, we also extract profiles of shallow cumulus clouds from the HAMP radar, with a cloud mask developed by segmenting the radar cloud data into individual two-dimensional cloud objects along time and height, which we refer to here as the Konow mask. All objects derived from the Konow mask with base below 1 km and top below 4 km are classified as shallow cumulus (ShCu) clouds. We estimate the fraction of radar echoes >-50 dBZ as a proxy for cloud fraction (CF) for the ShCu cloud objects as well as for all hydrometeors detected by the radar, and call them CFShCu and CFtotal, respectively.

We also use estimates of liquid water path (LWP) and rainwater path (RWP) from HAMP measurements by Jacob et al. (2019) to quantify cloud activity and precipitation,

[1] In boreal winter, we do not expect deep convective regimes in this area, and active situations might thus be associated with *disturbed* regimes and termed as such, whereas the more suppressed conditions are the *undisturbed* regimes. This is mentioned as a point of clarification to distinguish them from the corresponding terms "active" and "suppressed," used for the respective regions during the summer.

Brought to you by MAX-PLANCK-INSTITUTE FOR METEOROLOGY | Unauthenticated | Downloaded 07/20/21 01:00 PM UTC

TABLE 2. Details of the cloudiness parameters for the circles. Units are given in parentheses following parameter names. All parameters that do not have a "%" unit show mean values for the circle. Details of how the parameters are estimated are provided in section 2c.

	Flight ID							
	RF03		RF06		RF02		RF07	
Circle ID	S1	S2	S3	S4	A1	A2	A3	A4
Satellite CC (%)	1.2	7.8	11.9	16.0	11.4	55.1	92.5	61.1
Lidar CC (%)	11.9	17.8	17.5	17.4	—	—	52.3	47.1
Radar CC (%)	3.4	2.9	3.4	7.1	4.1	28.2	37.2	25.6
Peak ShCu CF (%)	0.3	1.3	0.7	4.0	1.5	10.5	1.0	0.8
RWP (g m^{-2})	7.0	2.9	2.7	10.1	2.5	20.7	8.5	15.2
RWP fraction (%)	0.0	0.1	0.1	0.8	0.1	3.4	2.4	4.4
LWP (g m^{-2})	165.1	132.3	129.8	200.1	126.3	201.1	105.4	207.9
LWP Fraction (%)	0.8	2.4	1.7	5.3	1.2	14.5	21.6	11.6
ShCu Top (m)	1254.0	1422.0	1410.0	1512.5	1211.2	1158.5	1496.0	1135.4
ShCu Base (m)	834.0	858.0	690.0	578.3	611.2	613.0	746.0	676.2

respectively. For LWP and RWP, only values > 50 g m^{-2} and > 1.5 g m^{-2}, respectively, are considered for both mean and fractions (see Table 2). This filter is to ensure that very low values that are likely noise are kept out of the estimation.

2) AIRBORNE LIDAR MEASUREMENTS

We also quantify cloudiness with the nadir-looking Water-vapor Lidar Experiment in Space (WALES) lidar (Wirth et al. 2009) on board HALO, from which estimates of cloud-top height (CTH) are retrieved by Gutleben et al. (2019), by setting a fixed threshold of 20 for the backscatter ratio at the 532 nm channel. The cloud cover over the flight path is estimated by calculating the fraction of lidar profiles that encountered a cloud from the total number of profiles. CTH values are not available for circles in RF02. For the rest of the circles, lidar coverage time exceeded 97% of the circle duration.

3) SATELLITE MEASUREMENTS

Since the radar and lidar measurements quantify clouds only over the circumference of the circle, we rely on satellite measurements to look at the cloudiness within the circle area (see Fig. 2). Hourly measurements at ~4 km (0.04°) horizontal resolution from Gridded Satellite (GridSat) from the *Geostationary Operational Environmental Satellite-13* (*GOES-13*) for the Western Hemisphere (GridSat-GOES) v01 (Knapp 2017) are used.

We follow the method of Benner and Curry (1998) to select cloudy pixels from satellite images using threshold values for channel 4 (brightness temperature from 11 μm channel) and channel 1 (reflectance from 0.6 μm band) for all circles. Since their method is applicable only to scattered cloudiness, such as in S-circles, we take the mean of the channel-4 thresholds for all S-circles, and apply this as a fixed threshold (295.59 K) across all circles to determine cloudy grid points and thus cloud cover (CC) in the circle area. This method works well under the assumption that the SST and LCL temperatures do not vary too much across the circles. Unlike the average channel-4 threshold, the channel-1 thresholds are still estimated individually for all circles. The cloud cover we estimate from satellites is only for the grid points that are completely within the circle or are overlapping the edges of the circle fitted to the dropsonde launch locations.

4) CUMULATIVE CLOUD-COVER PROFILES

Since the lidar and satellite cannot see past cloud tops, the cloud-cover profiles determined by the lidar and satellite are shown as cumulative profiles (see Fig. 3), with values increasing as altitude decreases, and the maximum value giving the total cloud cover for the circle area. For the satellite, since cloud detection is based on brightness temperatures and since these are not a monotonic function of height, we fit a mean temperature profile to altitude for every circle, by applying an isotonic linear regression (nonincreasing with height) to the respective circles' dropsonde temperature measurements.

d. Sampling scale

The above-mentioned environmental and cloud parameters are provided in Tables 1 and 2, respectively. The average lateral drift in the sondes was ~5 km in the direction of the mean flow, and hence, the displacement of the circle along the vertical profile can be considered negligible in terms of both the remotely sensed clouds and the environmental parameters sampled by the dropsondes. Also, since every round in a circle took around 45 min to 1 h, the environments and cloudiness of the circles characterized here should be taken as representative for the circles at a time scale of 1–2 h. Along with this time scale, the circles' average diameter of ~175 km also fits well with our objective of studying clouds and the environment at the mesoscale of ~20–200 km, which Orlanski (1975) calls the meso-β scale.

3. Characterizing the cloudiness

In this section, we sketch out what the clouds looked like for the different circles. For this, we resort to the aforementioned satellite measurements (Figs. 2 and 3), the radar measurements (Figs. 3, 4, and 5) and the lidar measurements (Fig. 3).

Brought to you by MAX-PLANCK-INSTITUTE FOR METEOROLOGY | Unauthenticated | Downloaded 07/20/21 01:00 PM UTC

a. Clouds in the S-circles

From Fig. 2, we see that circles S1 and S2 are part of a much larger, relatively homogeneous, cloud-free area, and thus have low CC_{circle} values. S3 is also mostly cloud-free, albeit with some bands of stratiform clouds at the northern and northeastern edges and a blanket of dust present toward the south—both also confirmed by visual testimony in the flight reports.

Both satellite and radar measurements show greater cloudiness in circle S4 compared to the other three S-circles, in terms of CC_{circle}, CF_{ShCu}, and CF_{total} (see Figs. 2–4 and Table 2). A perception of how active the clouds in these circles can be derived from the LWP and RWP estimates. Comparing the S-circles in Table 2 and Fig. 4, we see that S4 has more instances of relatively high LWP, and that its mean LWP is much higher than that of the other S-circles. The RWP also indicates that S4 has a greater number of precipitating clouds (large RWP fraction), with an overall higher intensity (larger mean RWP). Since the HAMP radar detects even low amounts of rain (Jacob et al. 2020), it would be fair to assume from Fig. 4, that S4 was the only S-circle along which any noticeable precipitation was measured.

In terms of lidar cloud cover (see Table 2), the S-circles do not vary much from each other except S1, which shows smaller values. This difference in cloudiness between the radar and lidar can be mostly explained by the difference in LWP values among the S-circles. Jacob et al. (2020) show that the HAMP radar misses more than 75% of the clouds detected by the WALES lidar, when LWP < 50 g m^{-2}. Thus, the lower LWP values of S1 through S3 result in the radar cloudiness deviating greatly from that of the lidar, as seen in the profiles in Fig. 3. Additionally, for S3, the lidar cloud cover also accumulates a distinct offset from the radar CF at an altitude of around ~1.7 km. This can be attributed to the presence of the stratiform clouds in the northern part of the circle, which were too shallow for the radar to detect. In contrast to the other S-circles, for S4 the radar is able to detect a larger proportion of the clouds detected by the lidar, indicating that most of the clouds in S4 were active clouds with relatively larger LWP.

The satellite cloud-cover profile in Fig. 3 shows that S4 had some clouds with tops reaching to ~3.5 km which are much higher than cloud tops in the other S-circles, which had maximum values of about 2 km. The general agreement between the satellite cloud cover and the radar measurements provides confidence that the airborne measurements were not simply sampling discrepancies. Thus, over several measures of cloudiness such as occurrence (CF and CC), activity (LWP and RWP) and vertical extent (cloud-top height), we find that circle S4 is significantly "cloudier" than the other three S-circles.

b. Clouds in the A-circles

A-circles show higher cloud tops (see gray regions in Fig. 2), and although A1 does not have any within the circle area itself, it is surrounded by similar spurts of high cloud tops. The HAMP radar gave echoes for parts of these cloud systems from surface up to the flight altitude (see Fig. 5), thus indicating that the high cloud tops we see from the satellite were indeed parts of deep convective clouds and their attached anvils. The greater spatial coverage (CC_{circle}) and higher cloud tops in A-circles (with the exception of A1) are in contrast to the S-circles, which are relatively cloud-free and have shallow clouds, with tops not exceeding brightness temperatures of ~288 K.

The contrast between S- and A-circles is also visible in cloud fraction profiles from the radar (Fig. 3). The peak low-level cloud fraction in the S-circles is at most one-sixth of that of the A2-A4 circles, and this could partially be explained also by the high LWP values obtained for the latter set of circles (see Fig. 5). The cloud fraction not only varies in amount, but also in its vertical structure. No cloudiness is observed above ~2 km, for the S-circles, whereas, for A-circles, the cloudiness can be observed up to flight level. A large proportion of clouds in A-circles have cloud tops much higher than 2 km, as shown in Fig. 5.

4. Relationship between the mesoscale environment and clouds

a. The thermodynamic environment

The dry, moist, and saturated moist static energy profiles in Fig. 3 together characterize the thermodynamic state of the atmosphere in the circles. The vertical structure of these profiles is consistent among the S-circles. All circles show the same features of well-mixed subcloud layers, a relatively dry free troposphere, and inversions present at ~1.6 km (indicated by the max N^2 line), which align well with the cloud tops from the remote sensing instruments. There are minor differences among the static energy profiles of the circles. However, these differences are more between days than across circles flown on the same day yet several hundreds of kilometers apart. As an example, consider the similarity among circles S3 and S4, both flown on the same day, a couple of hours apart. Both circles, compared to S1 and S2, show stronger inversions at ~1.8 km, as well as slightly less humidity and weaker stability at ~4–4.5 km. These differences indicate that the thermodynamic environments sampled are more homogeneous in space than they are stationary in time. In contrast, the variation in cloudiness among the S-circles (e.g., the greater cloudiness in S4) is on the mesoscale, and is not consistent for circles flown on the same day. Therefore, due to the similarity in its state across the large scale, the thermodynamics cannot be relied upon here to diagnose the mesoscale variability in cloudiness. With these observations, we thus find no support for the hypothesis that mean thermodynamic factors are adequate predictors of clouds for the mesoscale.

Upon analyzing conventional cloud-controlling factors for the S-circles, we find that the spread is small in the observed values for SST (27.9–29.4 °C), LTS (13–14 K), and PW (30–32 kg m^{-2}). For S4, none of these parameters has values that stand out as excessively large or small, compared to the other S-circles. Thus, the conventional cloud-controlling factors also fail to explain why S4 shows more cloudiness across several aspects. This indicates that although conventional cloud-controlling factors explain substantial variance on longer space and time scales, they are not as strongly correlated with the cloudiness at the mesoscale, which is consistent with

Brought to you by MAX-PLANCK-INSTITUTE FOR METEOROLOGY | Unauthenticated | Downloaded 07/20/21 01:00 PM UTC

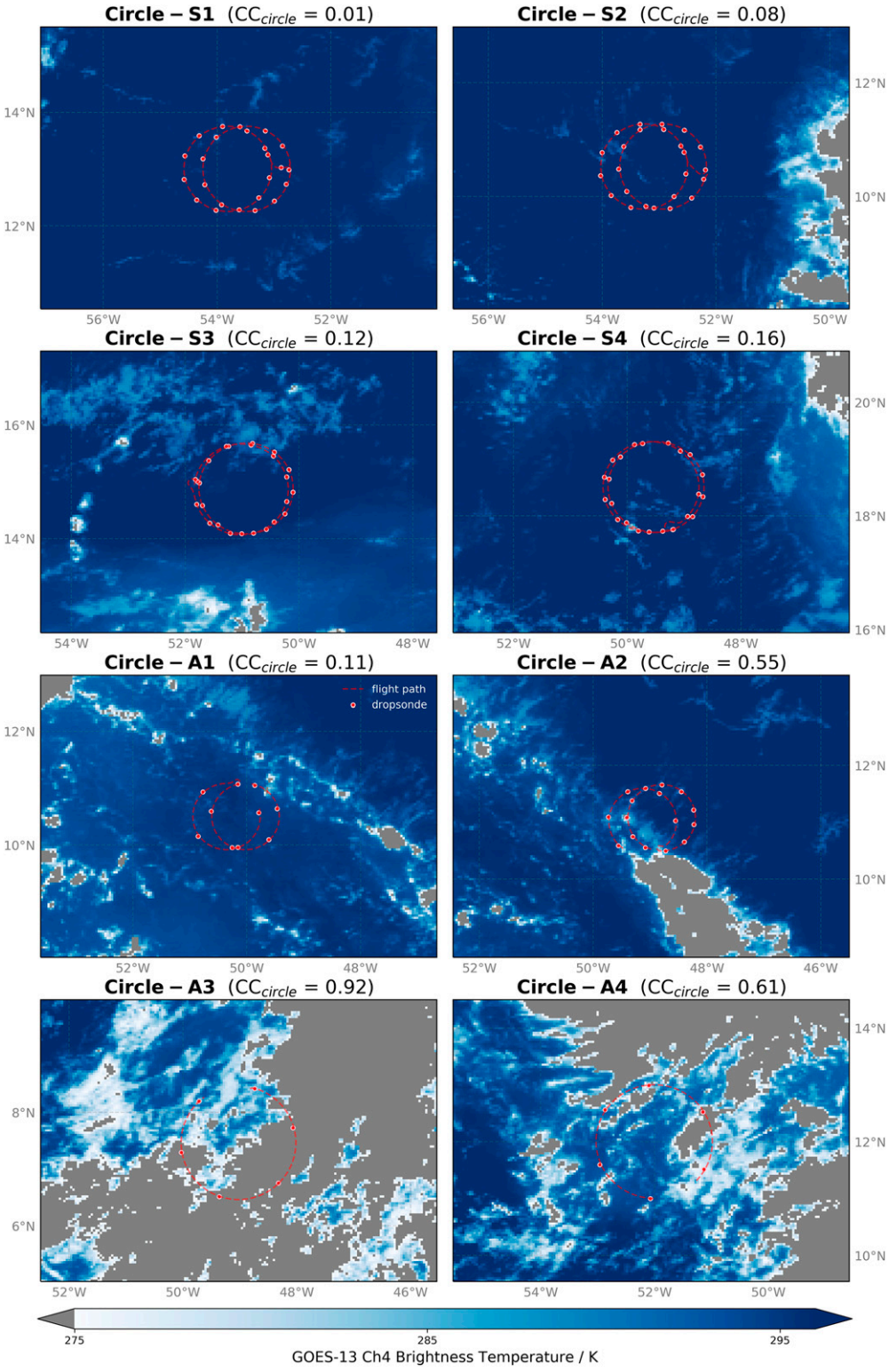

FIG. 2. The *GOES-13* channel-4 brightness temperature values are plotted for all circles, with the upper and lower limits on the color bar being the cloud detection threshold and indicator of deep convection, respectively. The red markers and lines show the dropsonde launch locations and the flight path, respectively. The time of satellite observation is the hour nearest to the circle mean time and the circle locations are shifted accordingly, following the mean wind. The CC_{circle} values over every box indicate the cloud cover within the circle area.

Brought to you by MAX-PLANCK-INSTITUTE FOR METEOROLOGY | Unauthenticated | Downloaded 07/20/21 01:00 PM UTC

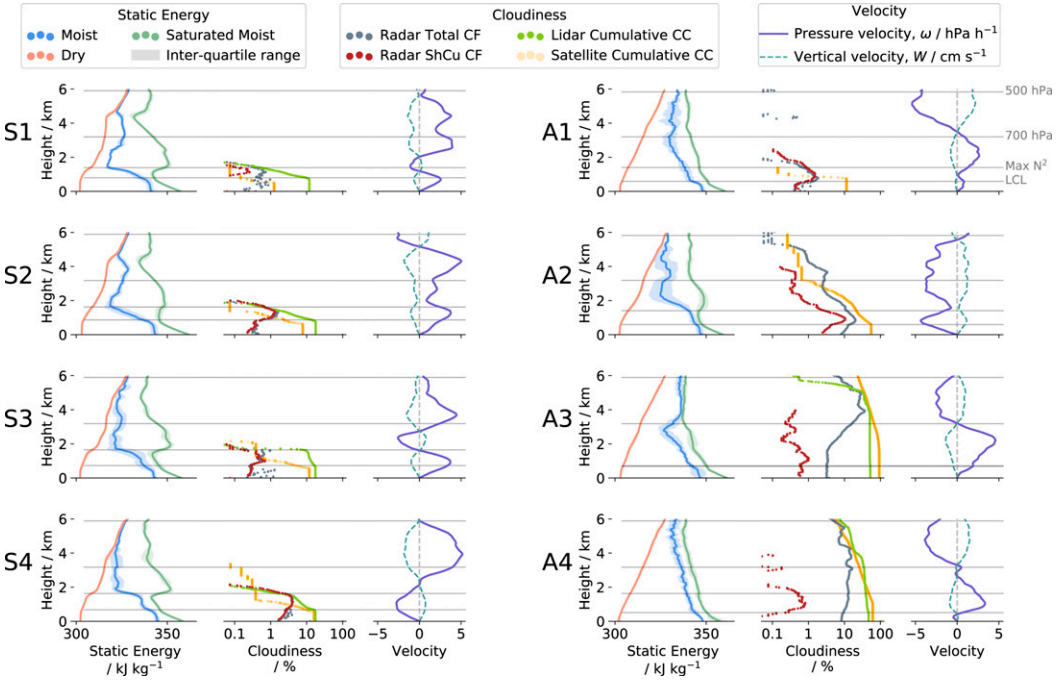

FIG. 3. For all circles, the (left) static energy profiles, (center) cloudiness profiles, and (right) the mesoscale vertical motion profiles are shown. The gray lines, cutting horizontally across all profiles are, from bottom to top, levels of LCL, maximum N^2, 700 hPa, and 500 hPa, for the particular circle. The static energy values, pressure velocity (ω), and vertical velocity (W) are determined from dropsonde measurements, and the cloudiness profiles are obtained from the HAMP radar, WALES lidar, and the GOES satellite, as per the legend.

findings of previous studies (e.g., Klein et al. 1995; Brueck et al. 2015; Nuijens et al. (2015a).

b. *Influence of subcloud vertical motion on mass flux*

An important, and we assert decisive, distinction among the S-circles is that for S4, the low-level flow is converging, leading to a layer of upward motion between the surface and ~2 km (see velocity profiles in Fig. 3). The other three S-circles show an almost completely subsiding layer from the surface to about 6 km. S4 is also the circle with largest values of shallow cumulus cloud fraction as well as cloud cover (see CF_{ShCu} in Fig. 3 and Table 2). Thus, since no thermodynamic component of the environment explains the large cloud amounts in S4, we hypothesize that the low-level convergence in S4 can provide a causal explanation. The convergence and subsequent upward vertical motion in the subcloud layer can exert its influence on clouds via the shallow convective mass flux (M). This hypothesis can also be extended to circle A2, which also has converging air masses in the subcloud layer and has the largest shallow cumulus cloud fraction. To test our hypothesis, we use a simple mass-flux estimate for the circles.

Vogel et al. (2020) demonstrate that M can be estimated as a residual of the subcloud-layer mass budget, relating M to the entrainment rate responsible for deepening the subcloud layer via small-scale mixing at its top (E) and mesoscale vertical velocity (W) at the top of the subcloud layer through the following budget equation:

$$\frac{\partial h}{\partial t} = E + W - M, \tag{1}$$

where $\partial h/\partial t$ is the rate of change of subcloud-layer depth. Following Vogel et al. (2020) we neglect the temporal change of h in the budget and estimate M as

$$M = E + W. \tag{2}$$

The shallow convective mass flux at any height z can also be estimated in a more direct manner by the equation

$$M(z) = a_{co}(z) w_{co}(z), \tag{3}$$

where a_{co} is the cloud-core area fraction occupied by clouds and w_{co} is the mean updraft velocity in the clouds. The cloud-core area fraction is defined as the fraction of the cloud area that has positive vertical velocity at cloud base. Combining Eqs. (2) and (3) gives us a relationship between cloud-core fraction at cloud base and the mesoscale vertical velocity as

$$a_{co} = \frac{E + W}{w_{co}}. \tag{4}$$

The estimates of mesoscale vertical velocity from the circle measurements are used to obtain W. Since the LCL can be taken as a proxy for the top of the subcloud layer, we take a mean value of the vertical velocity in a range of 50 m above and below the LCL as the value for W.

Brought to you by MAX-PLANCK-INSTITUTE FOR METEOROLOGY | Unauthenticated | Downloaded 07/20/21 01:00 PM UTC

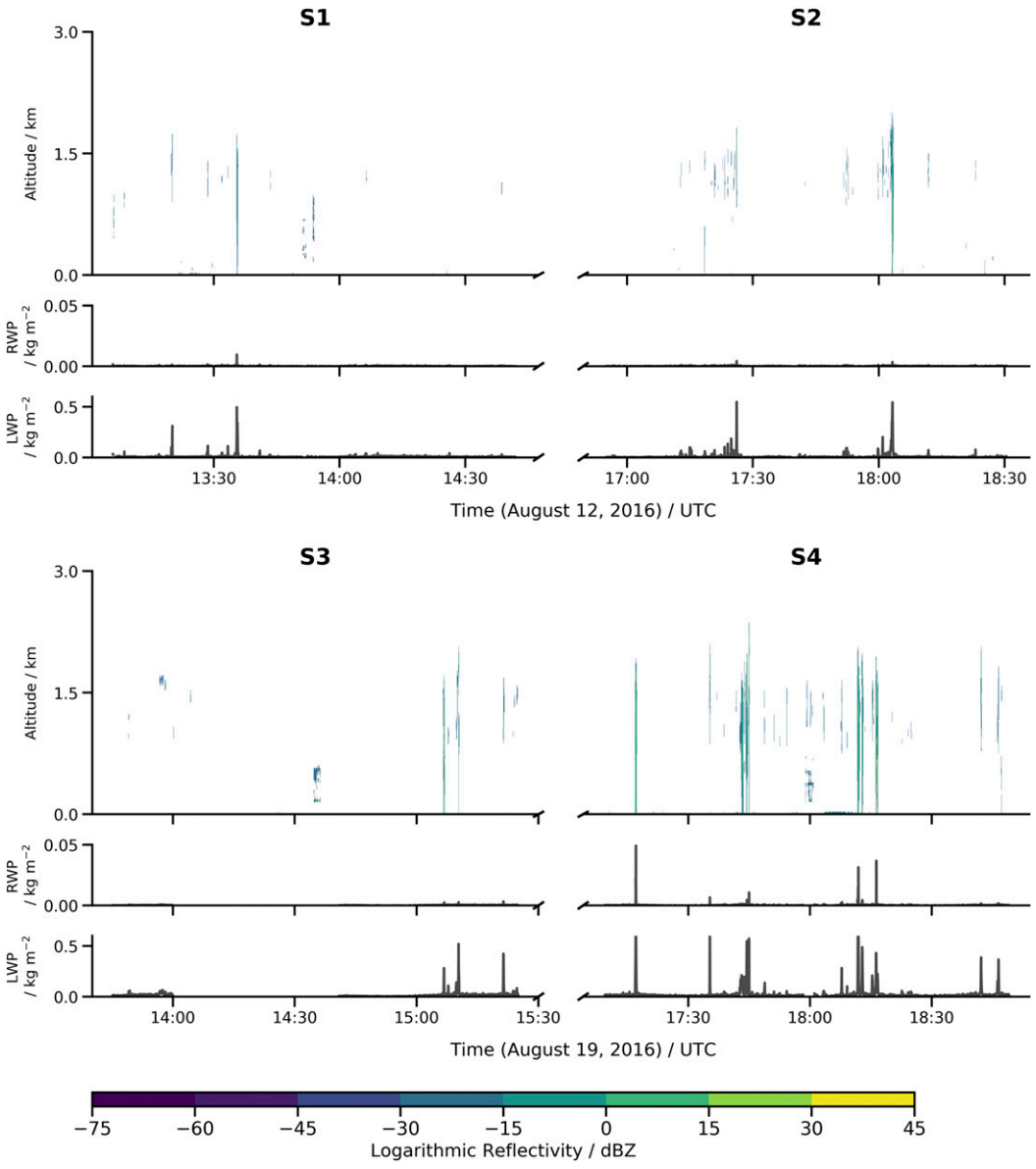

FIG. 4. (top) Radar reflectivity, (middle) rainwater path (RWP), and (bottom) liquid water path (LWP) are shown for all four S-circles.

To ensure a robust assumption for the values of E and w_{co}, we rely on findings from previous studies. Vogel et al. (2020) show that day-to-day variations in M are more correlated to variations in W than to variations in E. Following this, we assume a constant value of E for all circles. Vogel et al. (2020) obtain a mean value of 12.5 mm s^{-1} over the S-circles, and we take this as the value of E for all circles, with an uncertainty of $\pm$2.5 mm s^{-1}.

For core updraft velocities, we use the Deardorff convective velocity scale w^*, which is a good approximation for cloud-base convective updrafts over the ocean surface as shown by van Stratum et al. (2014) and Zheng (2019). The values of w^* are linearly related to the cloud-base height, or the LCL (Zheng and Rosenfeld 2015; Zheng 2019). With values of the LCL ranging between 510 and 865 m, we use values from the linear relationship shown by Zheng (2019) and assume a conservative range for variations in w_{co} from 0.4 to 0.8 m s^{-1}, with a mean of 0.6 m s^{-1}.

Thus, we theoretically estimate the cloud-core area fraction at cloud base by using the aforementioned values of W, E, and w_{co} as described by Eq. (4). The blue line in Fig. 6 shows predicted a_{co} and the shaded region indicates expected variability, for assumed variations in E and w_{co}. The peak shallow cumulus cloud fraction from the airborne HAMP radar has been overlaid on the theoretical estimates in Fig. 6. The peak values are usually found within a ~300 m deep layer above the LCL. It is important to note here that the theoretical cloud-core area fraction is only the area of cloud cover with positive updraft

Brought to you by MAX-PLANCK-INSTITUTE FOR METEOROLOGY | Unauthenticated | Downloaded 07/20/21 01:00 PM UTC

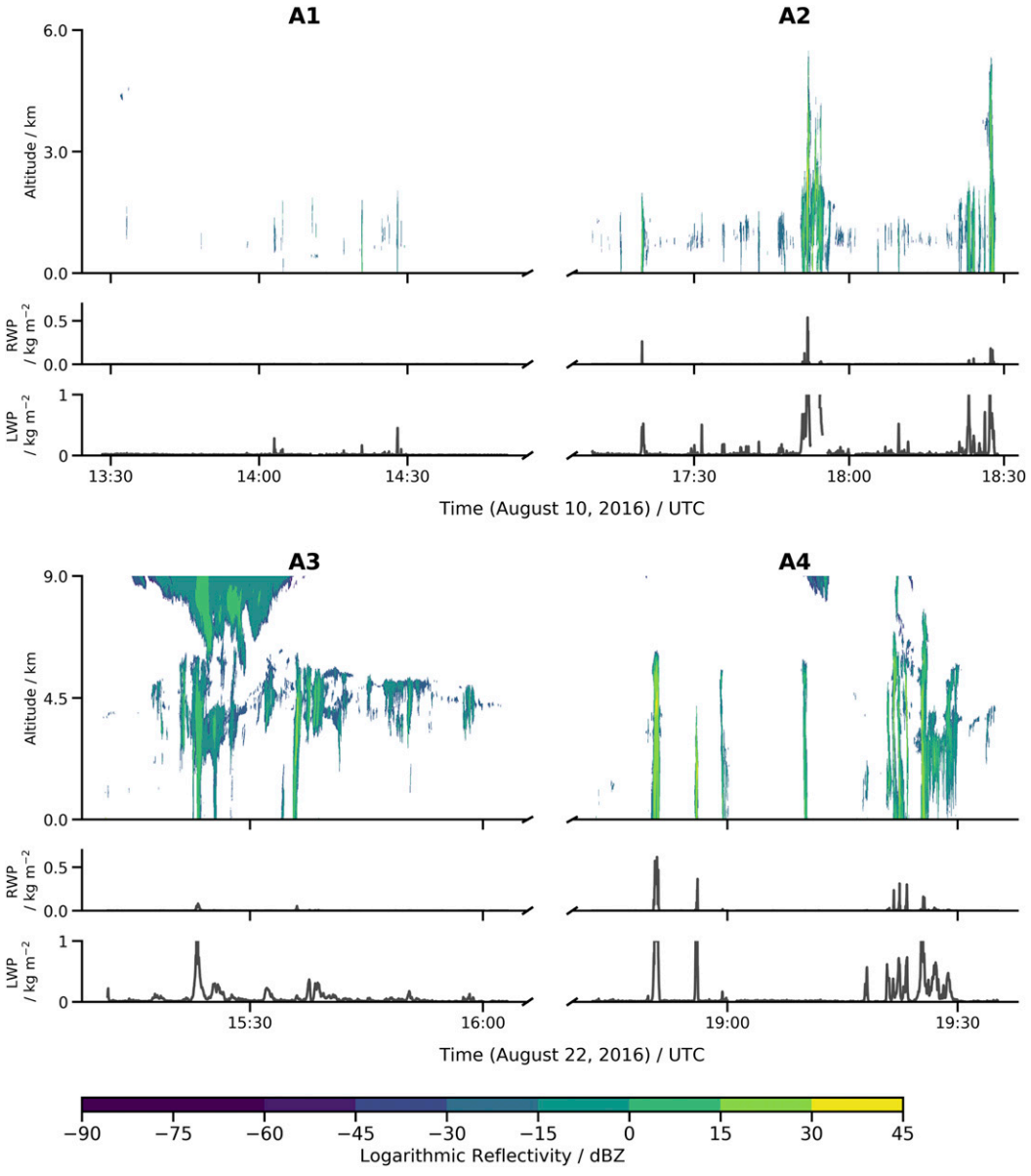

FIG. 5. (top) Radar reflectivity, (middle) rainwater path (RWP), and (bottom) LWP are shown for all four A-circles. Note that the scale of the Y axis is different for A1 and A2 versus A3 and A4 and also different from that in Fig. 4.

velocity at cloud base. The cloud fraction from the radar, however, is inclusive also of cloud areas that are negatively buoyant at cloud base, and thus, play no role in transporting mass outside the subcloud layer. The ratio of cloud core to total cloud cover has been empirically estimated to be 0.5 (Siebesma et al. 2003). Thus, the radar CF is expected to be greater than the estimated core fraction.

The CF values from the HAMP radar, however, are quite close to the predicted core fraction estimates. This is explained by the low sensitivity of the radar in detecting smaller clouds, and thus, giving lower cloud cover. Jacob et al. (2020) show that the HAMP radar could have missed an absolute value of ~7% of cloud fraction with radar reflectivity > -50 dBZ. Moreover, their study also shows that almost 75% of the clouds with LWP values $< 50\ \mathrm{g\ m^{-2}}$ were missed by the radar. This explains why the radar CF is underestimated. The cloud fraction of A2 is higher compared to the estimated core fraction. This is consistent with the higher LWP and RWP (see Table 2), which indicates a greater vertical development of the clouds rooted in the subcloud layer and that the majority of the clouds were captured by the radar.

Notwithstanding the difference in absolute values of estimated and actual fraction due to instrument limitations, the trend of the cloud fraction with respect to W is seen to be positive—similar to the theoretical estimation—thus lending

Brought to you by MAX-PLANCK-INSTITUTE FOR METEOROLOGY | Unauthenticated | Downloaded 07/20/21 01:00 PM UTC

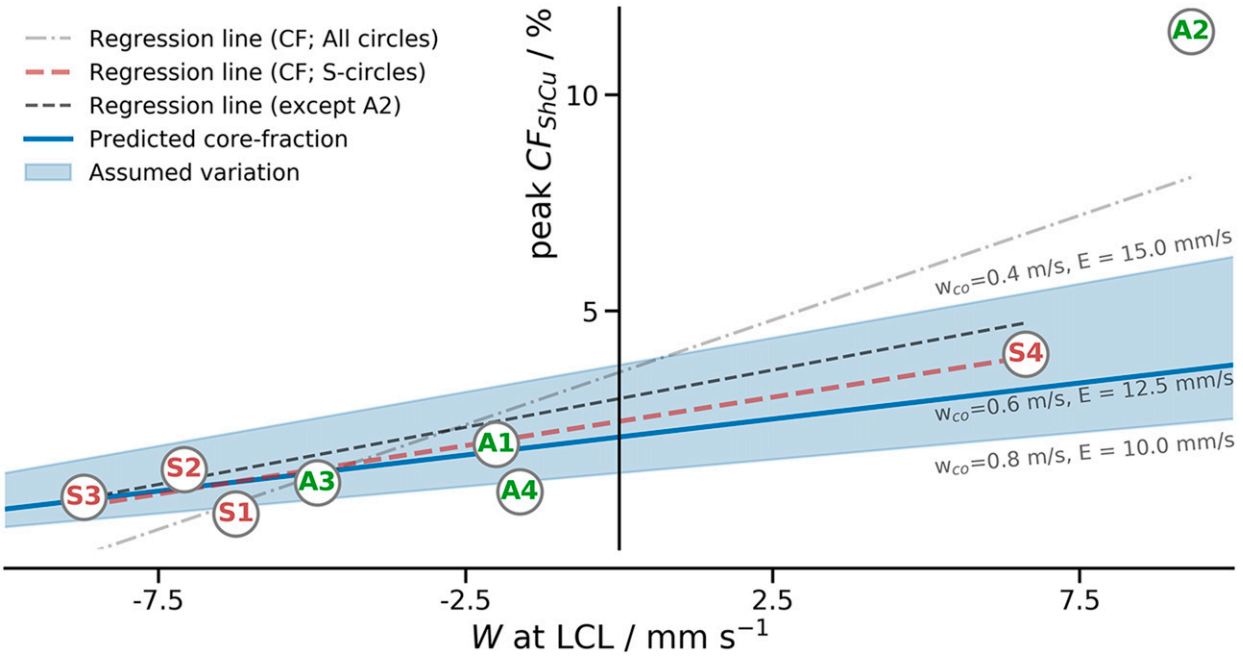

FIG. 6. Peak shallow cumulus cloud fraction (CF_{shcu}) from the radar is plotted against the large-scale vertical velocity at respective LCL heights of the circles. The shaded regions show range of estimated cloud-core fraction based on mass flux calculations (refer to the text in section 4b). The values of w_{co} and E used for prediction are shown as mean (below thick blue line) and bounds (adjacent to shaded envelope boundaries). The regression lines are lines of least squares fit for the data points indicated in the legend.

strength to our hypothesis that the mesoscale vertical velocity at LCL can influence cloud-base cloud fraction via the mass flux. These estimates thus provide a possible explanation as to why we see a higher cloud cover in S4 compared to the other S-circles. Clouds in S4 need to ventilate more air out of the mixed layer to balance the convergence of mass. This might be the cause for more active clouds in the region, with relatively higher LWP and RWP compared to the other S-circles. Even though subsidence reduces the mass flux for the other three S-circles, it is still not strong enough to offset the entrainment at the top of the mixed layer [Eq. (2)]. Hence, we still get positive values of mass flux and the prevalence of some cloudiness in the region, although much less than in the region with convergence (circle S4).

The primary takeaway from Fig. 6 thus is that the W scaling provides a possible explanation for the variability in shallow cumulus cloudiness. However, the relationship in the figure cannot be taken as that having statistical significance because of the small number of samples. Nevertheless, the positive relationship we see strengthens the argument in favor of our hypothesis that low-level convergence controls cloud fraction more instantaneously at the mesoscale than do thermodynamics—something that is also put forward by previous studies using reanalysis products (e.g., Mauger and Norris 2010; Myers and Norris 2013; de Szoeke et al. 2016).

We remind the reader that the values of cloud fraction plotted in Fig. 6 are only for shallow cumulus clouds. If the total cloud cover were shown instead, circles A3 and A4 would show a large increase, as can be understood from Fig. 7, which shows total cloud cover. Whereas Eq. (4) describes controls on cloud-base cloud fraction, it does not inform estimates of total cloud cover insofar as this is influenced by stratiform or other cloud processes aloft, e.g., the stratiform clouds pronounced in S3's lidar profile (Fig. 3) are not explained by the equation.

Another important takeaway from Fig. 6 is the linearity in the relationship between peak ShCu fraction and vertical velocity among the eight circles. However, if extrapolated toward values of larger negative W, this would not be linear any more, since cloudiness cannot be negative. This is important in light of how current cloud schemes deal with mesoscale variability. They attempt to account for variability on scales that are smaller than the gridscale for today's climate models (Sommeria and Deardorff 1977), but they do not specifically account for mesoscale (20–200 km) variability, such as that associated with the organization of shallow convection (Stevens et al. 2019b). Thus, in effect, cloud schemes assume that the mesoscale contributions average to zero. This assumption is valid only if the relationship between cloudiness and the mesoscale perturbations is linear. Thus, if there is large variability in mesoscale conditions, the assumption that the mesoscale influence would average to zero does not hold true because of the nonlinearity discussed above.

c. *Free-tropospheric vertical motion*

In contrast to W in the lower levels, W in the free troposphere has long been linked to cloudiness. In one of the earliest applications of this idea, Slingo (1987) demonstrated that ω in the upper troposphere can be an effective indicator of the synoptic regime and, consequently, can determine the cloud type prevailing in the region. Several studies since then have shown

Brought to you by MAX-PLANCK-INSTITUTE FOR METEOROLOGY | Unauthenticated | Downloaded 07/20/21 01:00 PM UTC

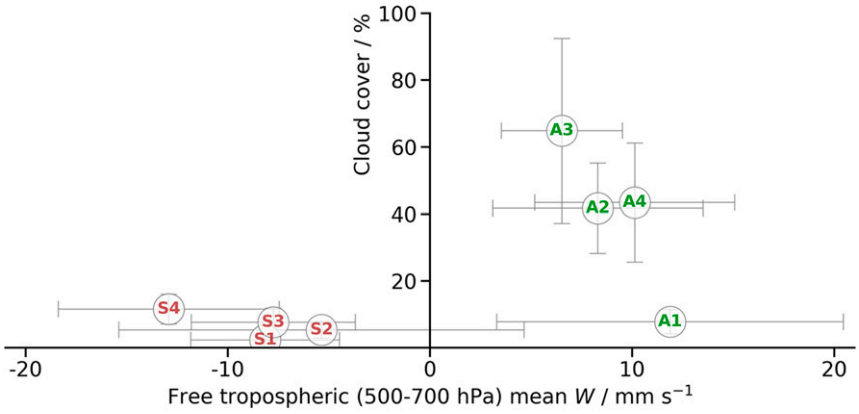

FIG. 7. Mean cloud cover from radar and satellite estimates of all circles plotted against the mean vertical velocity between pressure levels of 700 and 500 hPa. Horizontal bars show standard deviation of W and extents of the vertical bars show the lower and upper estimate of cloud cover, with these estimates being from the radar and the satellite, respectively, for all circles.

consistently how ω in the free troposphere influences time-averaged cloudiness over large ($\gg$200 km) spatial scales (e.g., Bony et al. 2004; Myers and Norris 2013). We test this idea for our "snapshots" of cloudiness on the mesoscale by associating the total cloud-cover estimates of the circle from the radar and satellite to the mean W (as a proxy for ω) in the free troposphere between pressure levels of 700 hPa and 500 hPa in Fig. 7.

The clustering of data points of A-circles away from that of S-circles in Fig. 7 shows the influence that ω in the free troposphere holds in setting the regime for cloudiness. However, this association becomes poor if taken for values of vertical velocity only at 500 hPa or only at 700 hPa (not shown), and serves as a hint that at the mesoscale, these values cannot be used as predictors (as previously suggested by Stevens and Brenguier 2009). This is especially true for the S-circles. If we want to correctly predict the differences in cloudiness among S-circles, just a measure of the standard ω_{500} or ω_{700} values are not enough, since a subsiding layer is a characteristic feature of the trade wind regions and will always be present.

Foregoing studies (e.g., Medeiros and Stevens 2009; Webb et al. 2015) have already noted this, stating that ω_{500} alone is not a good predictor of low-level cloudiness within subsidence regimes, and that LTS is a better predictor for these regimes. But from the NARVAL2 observations, we find that even both these predictors jointly are insufficient. Free-tropospheric ω (or W) helps distinguish between cloud types, but to distinguish between different extents of cloudiness within suppressed trade wind environments, focus should shift to factors that control cloudiness at the mesoscale. Therefore, in this sense, the vertical motion in the subcloud layer might hold more importance than that in the free troposphere.

5. Conclusions

We use estimates of mesoscale atmospheric vertical motion and collocated cloud measurements from the NARVAL2 campaign to understand the response of tropical clouds to their mesoscale environments. For this, we examine four cases each of low-level cloudiness forming in suppressed (S-circles) and active (A-circles) mesoscale environments.

Among the circles in the suppressed environments, circle S4 with air converging in its subcloud layer has greater cloudiness in terms of cloud fraction, liquid water path (LWP) and rainwater path (RWP). The only other circle, which also has a converging subcloud layer is A2, and it also shows large values of shallow cumulus cloud fraction, LWP, and RWP. From this association alone, it is difficult to establish if the convergence is causing the cloudiness or if it is a consequence of the cloudiness. In case of the latter though, we are left with no explanations for the cloudiness. Thus, in the absence of any thermodynamic factor that could explain the variation in cloudiness, we believe that the most plausible explanation for the increased cloudiness in S4 and A2 is the low-level convergence.

We find that large-scale parameters such as free-tropospheric ω or precipitable water can be useful in distinguishing between cloud regimes, such as shallow and deep convection. However, these are not helpful in distinguishing between the amount of cloudiness and its mesoscale variability within a given regime (e.g., suppressed). In this sense, the mesoscale dynamics proves to be more useful. We use a simple mass-flux estimate to show how the mesoscale vertical motion within the subcloud layer might regulate shallow cumulus cloud fraction at cloud base. This measure serves as a good indicator of shallow cloud amount across all flights, irrespective of thermodynamic state. Thus, the vertical velocity at the top of the subcloud layer helps explain variations in cloud-base cloud amounts that cannot otherwise be explained. While the relationship between mass flux and mesoscale vertical velocity for steady state has been emphasized previously (Vogel et al. 2020; Neggers et al. 2006), this is the first time we see a potential manifestation of it in nature through cloud area fraction at cloud base.

Although the relationship between mass flux and vertical velocity is linear, the same cannot be said for the relationship between cloudiness and vertical velocity, as cloudiness cannot be negative. This means that the response of clouds to their

Brought to you by MAX-PLANCK-INSTITUTE FOR METEOROLOGY | Unauthenticated | Downloaded 07/20/21 01:00 PM UTC

mesoscale circulation is nonlinear. Thus our results challenge the ansatz of general circulation model (GCM) parameterizations that the influence of the mesoscale circulation on cloudiness is inconsequential over larger scales. This outlook becomes especially important in the context of global warming, since any changes to the mesoscale circulation would not be reflected in the clouds, and will thus mask the changes in clouds and cloud feedbacks in a warming climate.

Our finding of the influence of mesoscale dynamics on clouds could also be considered to revisit strategies of estimating cloud fraction in climate models. Currently, all cloud parameterization schemes rely on thermodynamical variables to determine cloudiness. Although dynamics strongly influences thermodynamical variables, cloud schemes keep them out of direct consideration. Gridscale pressure velocity (ω) being a variable that already exists in GCMs, can be used to adjust parameterizations so as to depend also on mesoscale dynamics, along with the thermodynamic variables. Our results strengthen and provide observational support to the reasoning that dynamics needs to be incorporated directly into cloud schemes.

The NARVAL2 observations, although with a small sample size (eight circles), have the advantage of being well characterized in terms of their environment (thermodynamics and dynamics) as well as the cloudiness (radar, lidar, and satellite remote sensing), and sample regimes of both deep and shallow convection. With the limited sample size in mind, we do not provide a quantitative relationship between the variation in cloudiness and the vertical velocity. Instead, we put forward the argument that to understand the variability in mesoscale cloudiness, the circulation at that scale is something that we cannot ignore. Observations from the Elucidating the Role of Cloud-Circulation Coupling in Climate (EUREC^{4}A; Bony et al. 2017; Stevens et al. 2021) field campaign, which were focused on the trade wind suppressed regimes during January–February of 2020, will offer a larger statistical sampling of cloudiness and dynamical conditions, to quantify the variability in mesoscale conditions and thus help test the hypothesis we make. EUREC^{4}A will also provide more direct estimates of cloud-base cloud fraction and more robust estimates of the shallow convective mass flux.

Nevertheless, an advantage with the NARVAL2 cases is the sampling over active regimes. Our results provide observational evidence in favor of the argument that at the mesoscale, kinematic factors—such as subcloud mesoscale vertical velocity—can have greater control over low-level clouds than do thermodynamic factors, and as shown by both active and suppressed cases, this relationship does not seem to vary based on the regime of convection.

Acknowledgments. We thank the entire team of NARVAL2 for making the measurements. We thank Chris Fairall for sharing his code to compute the surface fluxes from the dropsondes. We thank Anna Lea Albright, Cathy Hohenegger, Theresa Mieslinger, Robert Pincus, and Hauke Schulz for their insights and helpful discussions. We thank Heike Konow for help with the cloud objects from the HAMP radar, which we refer to as the Konow mask in this study. We thank Manuel Gutleben and Martin Wirth for their help with the WALES lidar data and cloud-top height estimates using the same. This project has received funding from the European Research Council (ERC) project EUREC^{4}A (Grant 694768) under the European Union's Horizon 2020 research and innovation programme. ERA5 data were retrieved from the IPSL mesocenter ESPRI facility, which is supported by CNRS, Sorbonne Universite, Labex L-IPSL, CNES, and Ecole Polytechnique.

Data availability statement. The NARVAL2 measurements from the dropsondes, HAMP radar, and the HAMP microwave radiometers are available as unified data products from the CERA database at https://doi.org/10.1594/WDCC/HALO_measurements_3. The LWP and RWP products from the microwave measurements are available at the CERA database at https://doi.org/10.26050/WDCC/HALO_measurements_6. The WALES lidar data and the dropsondes raw data can be accessed from the HALO database http://doi.org/10.17616/R39Q0T. The GridSat-B1 satellite products are publicly available at https://www.ncei.noaa.gov/data/geostationary-ir-channel-brightness-temperature-gridsat-b1/access/. The ERA5 used in this study can be accessed from the ECMWF website (https://www.ecmwf.int/en/forecasts/datasets/reanalysis-datasets/era5).

REFERENCES

Augstein, E., H. Schmidt, and F. Ostapoff, 1974: The vertical structure of the atmospheric planetary boundary layer in undisturbed trade winds over the Atlantic Ocean. *Bound.-Layer Meteor.*, **6**, 129–150, https://doi.org/10.1007/BF00232480.

Benner, T. C., and J. A. Curry, 1998: Characteristics of small tropical cumulus clouds and their impact on the environment. *J. Geophys. Res.*, **103**, 28 753–28 767, https://doi.org/10.1029/98JD02579.

Bolton, D., 1980: The computation of equivalent potential temperature. *Mon. Wea. Rev.*, **108**, 1046–1053, https://doi.org/10.1175/1520-0493(1980)108<1046:TCOEPT>2.0.CO;2.

Bony, S., and J.-L. Dufresne, 2005: Marine boundary layer clouds at the heart of tropical cloud feedback uncertainties in climate models. *Geophys. Res. Lett.*, **32**, L20806, https://doi.org/10.1029/2005GL023851.

——, and B. Stevens, 2019: Measuring area-averaged vertical motions with dropsondes. *J. Atmos. Sci.*, **76**, 767–783, https://doi.org/10.1175/JAS-D-18-0141.1.

——, J.-L. Dufresne, H. Le Treut, J.-J. Morcrette, and C. Senior, 2004: On dynamic and thermodynamic components of cloud changes. *Climate Dyn.*, **22**, 71–86, https://doi.org/10.1007/s00382-003-0369-6.

——, and Coauthors, 2015: Clouds, circulation and climate sensitivity. *Nat. Geosci.*, **8**, 261–268, https://doi.org/10.1038/ngeo2398.

——, and Coauthors, 2017: EUREC4A: A field campaign to elucidate the couplings between clouds, convection and circulation. *Shallow Clouds, Water Vapor, Circulation, and Climate Sensitivity*, Space Sciences Series of ISSI, R. Pincus et al., Eds., Vol. 65, Springer, 357–396, https://doi.org/10.1007/978-3-319-77273-8_16.

Brueck, M., L. Nuijens, and B. Stevens, 2015: On the seasonal and synoptic time-scale variability of the North Atlantic trade wind region and its low-level clouds. *J. Atmos. Sci.*, **72**, 1428–1446, https://doi.org/10.1175/JAS-D-14-0054.1.

CDS, 2017: ERA5: Fifth generation of ECMWF atmospheric reanalyses of the global climate. Copernicus Climate Change Service, accessed 6 July 2020, https://cds.climate.copernicus.eu/cdsapp\#!/home.

Brought to you by MAX-PLANCK-INSTITUTE FOR METEOROLOGY | Unauthenticated | Downloaded 07/20/21 01:00 PM UTC

de Szoeke, S. P., K. L. Verlinden, S. E. Yuter, and D. B. Mechem, 2016: The time scales of variability of marine low clouds. *J. Climate*, **29**, 6463–6481, https://doi.org/10.1175/JCLI-D-15-0460.1.

Edson, J. B., and Coauthors, 2013: On the exchange of momentum over the open ocean. *J. Phys. Oceanogr.*, **43**, 1589–1610, https://doi.org/10.1175/JPO-D-12-0173.1.

Fairall, C. W., E. F. Bradley, J. E. Hare, A. A. Grachev, and J. B. Edson, 2003: Bulk parameterization of air–sea fluxes: Updates and verification for the COARE algorithm. *J. Climate*, **16**, 571–591, https://doi.org/10.1175/1520-0442(2003)016<0571:BPOASF>2.0.CO;2.

Gutleben, M., S. Groß, and M. Wirth, 2019: Cloud macro-physical properties in Saharan-dust-laden and dust-free North Atlantic trade wind regimes: A lidar case study. *Atmos. Chem. Phys.*, **19**, 10 659–10 673, https://doi.org/10.5194/acp-19-10659-2019.

Hersbach, H., and Coauthors, 2020: The ERA5 global reanalysis. *Quart. J. Roy. Meteor. Soc.*, **146**, 1999–2049, https://doi.org/10.1002/qj.3803.

Holland, J. Z., 1970: Preliminary report on the BOMEX sea-air interaction program. *Bull. Amer. Meteor. Soc.*, **51**, 809–821, https://doi.org/10.1175/1520-0477(1970)051<0809:PROTBS>2.0.CO;2.

Jacob, M., F. Ament, M. Gutleben, H. Konow, M. Mech, M. Wirth, and S. Crewell, 2019: Investigating the liquid water path over the tropical Atlantic with synergistic airborne measurements. *Atmos. Meas. Tech.*, **12**, 3237–3254, https://doi.org/10.5194/amt-12-3237-2019.

——, P. Kollias, F. Ament, V. Schemann, and S. Crewell, 2020: Multilayer cloud conditions in trade wind shallow cumulus—Confronting two ICON model derivatives with airborne observations. *Geosci. Model Dev.*, **13**, 5757–5777, https://doi.org/10.5194/gmd-2020-14.

Klein, S. A., 1997: Synoptic variability of low-cloud properties and meteorological parameters in the subtropical trade wind boundary layer. *J. Climate*, **10**, 2018–2039, https://doi.org/10.1175/1520-0442(1997)010<2018:SVOLCP>2.0.CO;2.

——, and D. L. Hartmann, 1993: The seasonal cycle of low stratiform clouds. *J. Climate*, **6**, 1587–1606, https://doi.org/10.1175/1520-0442(1993)006<1587:TSCOLS>2.0.CO;2.

——, ——, and J. R. Norris, 1995: On the relationships among low-cloud structure, sea surface temperature, and atmospheric circulation in the summertime northeast Pacific. *J. Climate*, **8**, 1140–1155, https://doi.org/10.1175/1520-0442(1995)008<1140:OTRALC>2.0.CO;2.

Knapp, K. R., 2017: Gridded satellite GOES coverage data (GridSat-GOES) Western Hemisphere v01. NOAA National Centers for Environmental Information, accessed 8 Aug 2019, https://doi.org/10.7289/V5HM56GM.

Konow, H., and Coauthors, 2019: A unified data set of airborne cloud remote sensing using the HALO Microwave Package (HAMP). *Earth Syst. Sci. Data*, **11**, 921–934, https://doi.org/10.5194/essd-11-921-2019.

Mapes, B. E., E. S. Chung, W. M. Hannah, H. Masunaga, A. J. Wimmers, and C. S. Velden, 2018: The meandering margin of the meteorological moist tropics. *Geophys. Res. Lett.*, **45**, 1177–1184, https://doi.org/10.1002/2017GL076440.

Mauger, G. S., and J. R. Norris, 2010: Assessing the impact of meteorological history on subtropical cloud fraction. *J. Climate*, **23**, 2926–2940, https://doi.org/10.1175/2010JCLI3272.1.

Mech, M., E. Orlandi, S. Crewell, F. Ament, L. Hirsch, M. Hagen, G. Peters, and B. Stevens, 2014: HAMP—The microwave package on the High Altitude and Long Range research aircraft (HALO). *Atmos. Meas. Tech.*, **7**, 4539–4553, https://doi.org/10.5194/amt-7-4539-2014.

Medeiros, B., and B. Stevens, 2009: Revealing differences in GCM representations of low clouds. *Climate Dyn.*, **36**, 385–399, https://doi.org/10.1007/s00382-009-0694-5.

Myers, T. A., and J. R. Norris, 2013: Observational evidence that enhanced subsidence reduces subtropical marine boundary layer cloudiness. *J. Climate*, **26**, 7507–7524, https://doi.org/10.1175/JCLI-D-12-00736.1.

Neggers, R., B. Stevens, and J. D. Neelin, 2006: A simple equilibrium model for shallow-cumulus-topped mixed layers. *Theor. Comput. Fluid Dyn.*, **20**, 305–322, https://doi.org/10.1007/s00162-006-0030-1.

Nuijens, L., B. Medeiros, I. Sandu, and M. Ahlgrimm, 2015a: The behavior of trade-wind cloudiness in observations and models: The major cloud components and their variability. *J. Adv. Model. Earth Syst.*, **7**, 600–616, https://doi.org/10.1002/2014MS000390.

——, ——, ——, and ——, 2015b: Observed and modeled patterns of covariability between low-level cloudiness and the structure of the trade-wind layer. *J. Adv. Model. Earth Syst.*, **7**, 1741–1764, https://doi.org/10.1002/2015MS000483.

Orlanski, I., 1975: A rational subdivision of scales for atmospheric processes. *Bull. Amer. Meteor. Soc.*, **56**, 527–530, https://doi.org/10.1175/1520-0477-56.5.527.

Qu, X., A. Hall, S. A. Klein, and A. M. DeAngelis, 2015: Positive tropical marine low-cloud cover feedback inferred from cloud-controlling factors. *Geophys. Res. Lett.*, **42**, 7767–7775, https://doi.org/10.1002/2015GL065627.

Siebesma, A. P., and Coauthors, 2003: A large eddy simulation intercomparison study of shallow cumulus convection. *J. Atmos. Sci.*, **60**, 1201–1219, https://doi.org/10.1175/1520-0469(2003)60<1201:ALESIS>2.0.CO;2.

Slingo, J. M., 1987: The development and verification of a cloud prediction scheme for the ECMWF model. *Quart. J. Roy. Meteor. Soc.*, **113**, 899–927, https://doi.org/10.1002/qj.49711347710.

Sommeria, G., and J. W. Deardorff, 1977: Subgrid-scale condensation in models of nonprecipitating clouds. *J. Atmos. Sci.*, **34**, 344–355, https://doi.org/10.1175/1520-0469(1977)034<0344:SSCIMO>2.0.CO;2.

Stevens, B., and J.-L. Brenguier, 2009: Cloud-controlling factors: Low clouds. *Clouds in the Perturbed Climate System: Their Relationship to Energy Balance, Atmospheric Dynamics, and Precipitation*, J. Heintzenberg and R. J. Charlson, Eds., MIT Press, 173–196.

——, A. Beljaars, S. Bordoni, C. Holloway, M. Köhler, S. Krueger, V. Savic-Jovcic, and Y. Zhang, 2007: On the structure of the lower troposphere in the summertime stratocumulus regime of the northeast Pacific. *Mon. Wea. Rev.*, **135**, 985–1005, https://doi.org/10.1175/MWR3427.1.

——, and Coauthors, 2019a: A high-altitude long-range aircraft configured as a cloud observatory: The NARVAL expeditions. *Bull. Amer. Meteor. Soc.*, **100**, 1061–1077, https://doi.org/10.1175/BAMS-D-18-0198.1.

——, and Coauthors, 2019b: Sugar, gravel, fish and flowers: Mesoscale cloud patterns in the trade winds. *Quart. J. Roy. Meteor. Soc.*, **146**, 141–152, https://doi.org/10.1002/qj.3662.

——, and Coauthors, 2021: EUREC^{4}A. *Earth Syst. Sci. Data*, https://doi.org/10.5194/essd-2021-18, in press.

van Stratum, B. J. H., J. Vilá-Guerau de Arellano, C. C. van Heerwaarden, and H. G. Ouwersloot, 2014: Subcloud-layer feedbacks driven by the mass flux of shallow cumulus convection over land. *J. Atmos. Sci.*, **71**, 881–895, https://doi.org/10.1175/JAS-D-13-0192.1.

Vogel, R., S. Bony, and B. Stevens, 2020: Estimating the shallow convective mass flux from the subcloud-layer mass budget.

Brought to you by MAX-PLANCK-INSTITUTE FOR METEOROLOGY | Unauthenticated | Downloaded 07/20/21 01:00 PM UTC

J. Atmos. Sci., **77**, 1559–1574, https://doi.org/10.1175/JAS-D-19-0135.1.

Wang, J. J., and Coauthors, 2015: A long-term, high-quality, high-vertical-resolution GPS dropsonde dataset for hurricane and other studies. *Bull. Amer. Meteor. Soc.*, **96**, 961–973, https://doi.org/10.1175/BAMS-D-13-00203.1.

Webb, M. J., and Coauthors, 2015: The impact of parametrized convection on cloud feedback. *Philos. Trans. Roy. Soc.*, **373A**, 20140414, https://doi.org/10.1098/rsta.2014.0414.

Wirth, M., A. Fix, P. Mahnke, H. Schwarzer, F. Schrandt, and G. Ehret, 2009: The airborne multi-wavelength water vapor differential absorption lidar WALES: System design and performance. *Appl. Phys.*, **96B**, 201–213, https://doi.org/10.1007/s00340-009-3365-7.

Zelinka, M. D., T. A. Myers, D. T. McCoy, S. Po-Chedley, P. M. Caldwell, P. Ceppi, S. A. Klein, and K. E. Taylor, 2020: Causes of higher climate sensitivity in CMIP6 models. *Geophys. Res. Lett.*, **47**, e2019GL085782, https://doi.org/10.1029/2019GL085782.

Zheng, Y., 2019: Theoretical understanding of the linear relationship between convective updrafts and cloud-base height for shallow cumulus clouds. Part I: Maritime conditions. *J. Atmos. Sci.*, **76**, 2539–2558, https://doi.org/10.1175/JAS-D-18-0323.1.

——, and D. Rosenfeld, 2015: Linear relation between convective cloud base height and updrafts and application to satellite retrievals. *Geophys. Res. Lett.*, **42**, 6485–6491, https://doi.org/10.1002/2015GL064809.

Brought to you by MAX-PLANCK-INSTITUTE FOR METEOROLOGY | Unauthenticated | Downloaded 07/20/21 01:00 PM UTC